論文 / 著書情報
Article / Book Information

Title	Additive manufacturing of γ’ precipitate-strengthened nickel-based superalloy UNS N07001 by electron beam melting: Effects of post-heat treatment on microstructure and mechanical properties
Authors	Ryo Takakuwa, Motoki Sakaguchi, Yuante Chin, Hiroaki Nakamoto, Manabu Noguchi, Hirotsugu Inoue
Citation	Additive Manufacturing, Vol. 100, , 104690
Pub. date	2025, 2
DOI	https://dx.doi.org/10.1016/j.addma.2025.104690
Creative Commons	Information is in the article.

Additive Manufacturing 100 (2025) 104690

Contents lists available at ScienceDirect

Additive Manufacturing

journal homepage: www.elsevier.com/locate/addma

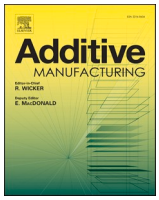

Additive manufacturing of γ' precipitate-strengthened nickel-based superalloy UNS N07001 by electron beam melting: Effects of post-heat treatment on microstructure and mechanical properties

Ryo Takakuwa [a,b,*], Motoki Sakaguchi [b], Yuante Chin [a], Hiroaki Nakamoto [a], Manabu Noguchi [a], Hirotsugu Inoue [b]

[a] Technologies & Intellectual Property Division, Ebara Corporation, 4-2-1 Honfujisawa, Fujisawa-shi, Kanagawa 251-8502, Japan
[b] School of Engineering, Department of Mechanical Engineering, Institute of Science Tokyo (Tokyo Institute of Technology), 2-12-1 Ookayama, Meguro-ku, Tokyo 152-8552, Japan

ARTICLE INFO

Keywords:
Powder bed fusion
Electron beam melting
Process parameter optimization
Nickel-based superalloy
Microstructure
Mechanical properties

ABSTRACT

The γ' precipitate-strengthened nickel-based superalloy UNS N07001 is widely used in gas turbines because of its high-temperature strength and corrosion resistance. In this paper, optimal process parameters of electron beam melting were determined to shorten the lead time of UNS N07001. In addition, the effects of post-heat treatment on the microstructure and mechanical properties of UNS N07001 were evaluated. The optimal process parameters were determined by evaluating the appearance, surface roughness, relative density, and Brinell hardness of UNS N07001 blocks built with 32 different parameter combinations. The UNS N07001 sample produced using the optimal parameters was subjected to hot isotropic pressing (HIP) and solution treatment and aging (STA). Microstructural observation, precipitate analysis, and tensile tests of the resulting specimens were conducted. Microstructural observations and precipitate analysis revealed that the as-built specimen contained cracks and pores. These defects disappeared after HIP treatment. Additionally, STA after HIP treatment resulted in a high content of fine γ'-phase precipitate. Tensile tests revealed that the mechanical properties of the specimen were barely changed by HIP treatment, whereas STA after HIP markedly improved the mechanical properties of the specimen to a level comparable to the requirements for the wrought material. The beneficial mechanical properties of the specimen treated by HIP and STA may be attributed to the high content of fine γ' precipitates.

1. Introduction

The γ' precipitate-strengthened Ni-based superalloy UNS N07001 (Ni–13.5Co–19Cr-4.3Mo–1.5Al–3Ti–0.08C–0.006B–0.05Zr, mass%) is widely used in gas turbines because of its high-temperature strength and corrosion resistance. UNS N07001 contains Mo, Co, and Cr as solid solution strengthening elements and Ti and Al as precipitation strengthening elements. Heat treatment of UNS N07001 generally involves solution treatment followed by a two-step aging process, which is important to ensure stable precipitation of the γ' phase. The mechanical properties of UNS N07001 are useful at temperatures up to ~980 °C, comparable to those of other Ni-based superalloys, such as Rene 41, and generally better than those of Alloy 718 at temperatures above 650 °C.

A common manufacturing method of UNS N07001 is forging, which requires a long lead time. Additive manufacturing (AM) is a new manufacturing technology that shortens lead time because of its fast production speed. AM is a bottom-up technology for constructing three-dimensional (3D) objects by adding materials based on 3D model data, which is in contrast to top-down processes based on subtraction like machining. In the early days of AM, rapid prototyping using resin was common. Recently, AM has been attracting attention from industry because it has become possible to construct metallic materials with high melting points and ceramics. AM was standardized by the American Society for Testing and Materials (ASTM) in 2009 and classified into seven categories: binder jetting (BJT), directed energy deposition (DED), material extrusion, material jetting, powder bed fusion (PBF), sheet lamination, and vat photopolymerization [1]. Regarding each AM method, BJT, DED, and PBF have been applied to metallic materials.

* Corresponding author at: Technologies & Intellectual Property Division, Ebara Corporation, 4-2-1 Honfujisawa, Fujisawa-shi, Kanagawa 251-8502, Japan.
E-mail addresses: takakuwa.ryo@ebara.com (R. Takakuwa), sakaguchi.m.ac@m.titech.ac.jp (M. Sakaguchi), chin.yuante@ebara.com (Y. Chin), nakamoto.hiroaki@ebara.com (H. Nakamoto), noguchi.manabu@ebara.com (M. Noguchi), inoue.h.ab@m.titech.ac.jp (H. Inoue).

https://doi.org/10.1016/j.addma.2025.104690
Received 29 October 2024; Received in revised form 18 January 2025; Accepted 3 February 2025
Available online 4 February 2025

Among these methods, DED and PBF are used to melt metals directly. DED is suitable for manufacturing large-sized products with relatively simple shapes, whereas PBF is suitable for manufacturing complex shapes with high precision, although it has limitations with respect to product size. In DED, parts are built by simultaneously irradiating metal or other material powder with a laser or electron beam to melt the material. In PBF, metal powder is laid down and then irradiated by a laser or electron beam, which causes melting in the built area. PBF has attracted attention as the leading AM technology for metal materials.

PBF can be further divided into electron beam PBF (EB-PBF) and laser beam PBF (LB-PBF). Each type has advantages and disadvantages. EB-PBF has a higher output than LB-PBF, resulting in a faster scan speed. When a metal powder is irradiated by an electron beam, the powder becomes charged, generating a smoke in which the powder particles repel each other and diffuse. In EB-PBF, the powder is preheated and sintered before the melting process of each layer to prevent smoke formation. Therefore, EB-PBF has smaller temperature variation during building and lower thermal stress compared with that of LB-PBF. As a result, the products built with EB-PBF contain fewer internal cracks induced by the residual stress during the construction process than those produced by LB-PBF. In LB-PBF, the lower output of the laser and smaller powder particle size allow the product to possess a smooth surface, so LB-PBF is suitable for building complex structures.

Regarding difficulty and technical issues, PBF is similar to welding, which involves melting and solidifying metallic materials. Therefore, alloys with poor weldability are difficult to use in AM [2]. In the welding of Ni-based superalloys, high-temperature cracking and reheat cracking can be problematic. High-temperature cracking occurs during welding and can be roughly classified into solidification cracking in the weld metal and liquefaction cracking in the heat-affected zone. Reheat cracking occurs during the heat treatment process after welding or during the operation period of the welded structure. In the case of Ni-based superalloys, a higher content of the γ' phase increases the likelihood of reheat cracking [3], which generally occurs during the solid solution treatment to induce γ'-phase precipitation. The reheat cracking of UNS N07001 has been studied [4,5]. Quin and co-workers investigated the susceptibility of wrought UNS N07001 to liquation cracking in the heat-affected zone by performing Gleeble hot ductility testing [6]. They found that the intergranular cracking behavior of UNS N07001 was affected by long-term isothermal heat treatment.

Alloy 718 is a Ni-based superalloy that is commonly used in AM because of its high weldability. Unlike γ' precipitation-strengthened alloys, Alloy 718 has low Ti and Al contents and a high Nb content. The main strengthening factor of Alloy 718 is the γ" phase, which means that Alloy 718 has better weldability than γ' precipitate-strengthened alloys, making it suitable for AM. Many studies on Alloy 718 built by PBF have been conducted, including investigating the effects of process parameters on microstructure [7–9], post-heat treatment on microstructure and mechanical properties [10–13], post-heat treatment and building direction on creep properties [14–16], and post-heat treatment and surface treatment on fatigue properties [17–19].

Many studies on the PBF of non-weldable Ni-based superalloys have also been conducted. In research on precipitation-strengthened superalloy CM247LC manufactured by LB-PBF, it was found that microcrack content was decreased by optimizing the production process and decreasing the amount of Hf added [20–23]. The mechanical and creep properties of CM247LC produced by LB-PBF have also been studied [24,25]. Recently, Rene 41, which has similar chemical composition and mechanical properties to those of UNS N07001, has also attracted attention. Atabay et al. [26,27] evaluated the effect of post-heat treatment on the microstructure and mechanical properties of Rene 41 built by LB-PBF. They found that post-heat treatment induced precipitation of the γ' phase and increased strength and that heat treatment at the sub-solvus temperature of the γ' phase improved the elongation of the heat-treated product. Several investigations have been conducted on EB-PBF for Haynes 282, a derivative alloy of UNS N07001. Unocic et al. achieved a nearly fully dense material by varying the process parameters and found that post-heat treatment significantly improved the mechanical properties at high temperatures [28]. Singh et al. investigated the microstructural evolution along the building direction during EB-PBF and revealed that Haynes 282 built by EB-PBF exhibits higher tensile strength and yield strength but lower elongation than the as-received wrought alloy [29].

As explained above, considerable research has been conducted on Alloy 718 built by PBF. However, there has been comparatively little research on AM of UNS N07001. Jedynak and colleagues evaluated the microstructure and hot workability of UNS N07001 built by LB-PBF by comparison with the properties of the wrought material, but the mechanical properties of the material were not evaluated [30]. Recently, Sazerat et al. [31] investigated the microstructural stability of UNS N07001 built by wire arc AM at high temperatures. However, there are no studies on UNS N07001 built by EB-PBF. It is essential to optimize the process parameters of EB-PBF of UNS N07001 to make AM practical as a manufacturing method for this superalloy. In this study, the process parameters of EB-PBF are optimized for UNS N07001. Post-heat treatment is performed on UNS N07001 built using the optimal process parameters, allowing the effect of post-heat treatment on the microstructure and mechanical properties of UNS N07001 to be evaluated.

2. Materials and methods

2.1. Materials

UNS N07001 powder manufactured by gas atomization was used as the raw material for EB-PBF. Table 1 lists the chemical composition of UNS N07001 (mass%). Fig. 1 shows the surface morphology of UNS N07001 powder observed by scanning electron microscopy (SEM; JEOL JSM-6610, Tokyo, Japan). The sphericity of the UNS N07001 powder particles was high. Fig. 2 presents the particle size distribution of the UNS N07001 powder. The grain size was concentrated in the range of 50–150 μm, with an average particle size of approximately 80 μm. In general, powders with a grain size of 40–105 μm are suitable for EB-PBF [2].

2.2. Fabrication of UNS N07001 parts by EB-PBF

An Arcam EB-PBF 3D printer A2X was used to build UNS N07001 parts. In EB-PBF, a 3D structure is built by repeating the process of scanning the electron beam and melting/solidifying one layer of metal powder based on 3D CAD data loaded into the machine. Fig. 3 shows a schematic diagram of the scan strategy. Blocks with dimensions of 15 mm × 15 mm × 20 mm were built by EB-PBF. A total of 32 different process parameters were used in block construction. The electron beam current and scanning speed were varied from 3.8 to 5.3 mA and 175–265 mm/s, respectively, as summarized in Table 2. An acceleration voltage of the electron beam of 60 kV, hatch spacing (line offset of the electron beam) of 0.125 mm, powder layer thickness of 75 μm, and preheating temperature of 1025 °C were used. The electron beam direction was rotated 90° for each layer.

Fig. 4 shows photographs of the batches of blocks produced under different conditions. There were two batches of 16 blocks each. The optimal process parameters were investigated by evaluating the surface morphology, surface roughness, relative density, and Brinell hardness of the blocks. Surface morphology and surface roughness were measured using a 3D profiler (Keyence VR-3200, Osaka, Japan). Density was

Table 1
Chemical composition of UNS N07001 (mass%).

Cr	Co	Mo	C	Zr	B	Ti	Al	Ni
20	13.5	4.3	0.03	0.06	0.005	3	1.5	Bal.

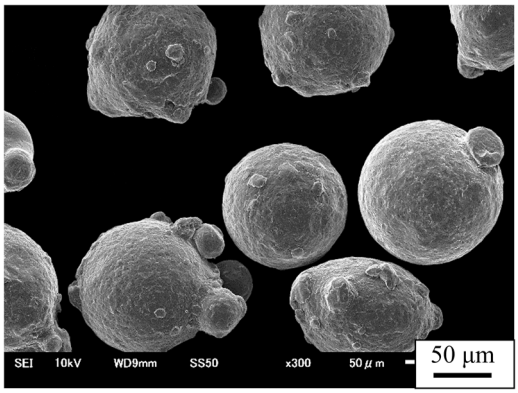

Fig. 1. SEM image of the UNS N07001 gas-atomized powder.

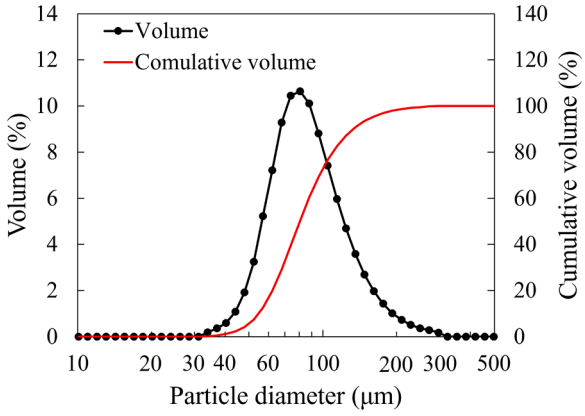

Fig. 2. Particle size distribution of the UNS N07001 gas-atomized powder.

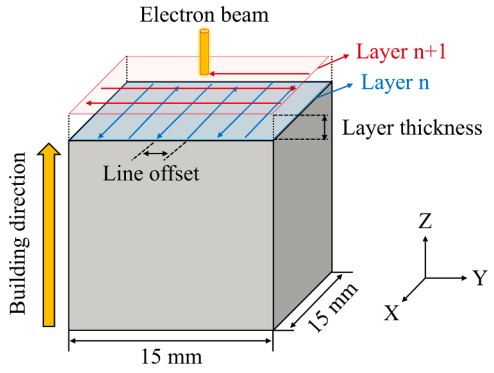

Fig. 3. Schematic diagram of the scan strategy and part of a 15 mm × 15 mm × 20 mm block built by EB-PBF.

measured using the Archimedes' principle according to ASTM B311–17. The weights of the blocks in air and water were measured using an electronic balance (Shimadzu AUX-220, Kyoto, Japan). Relative density (ρ_r) was calculated using the theoretical density of 8.20 g/cm^3 for UNS N07001. Brinell hardness tests were performed using a Brinell hardness tester (Kansai Kiki Manufacturing, Osaka, Japan) to evaluate the mechanical properties of the blocks. The measurement point was near the center of each block using a load of 750 kgf and an indenter diameter of 5 mm. The test method was conducted in accordance with ASTM E10. Hardness tests were conducted at room temperature (RT).

Table 2
Process parameters for block construction.

Sample No.	Current (mA)	Scan speed (mm/s)	Sample No.	Current mA	Scan speed (mm/s)
1	5.30	175	17	4.65	235
2	5.30	205	18	4.65	265
3	5.30	235	19	4.50	215
4	5.30	265	20	4.50	225
5	4.80	175	21	4.50	235
6	4.80	205	22	4.50	245
7	4.80	235	23	4.50	255
8	4.80	265	24	4.50	265
9	4.30	175	25	4.30	215
10	4.30	205	26	4.30	225
11	4.30	235	27	4.15	175
12	4.30	265	28	4.15	190
13	3.80	175	29	4.15	205
14	3.80	205	30	4.00	175
15	3.80	235	31	4.00	190
16	3.80	265	32	4.00	205

2.3. Specimen preparation and evaluation with optimal parameters

The results of the evaluation of the 32 blocks produced under different conditions suggested that No. 25 was built using the optimal process parameters (details of this evaluation are given in Section 3.1). Next, 20 mm × 20 mm × 100 mm bars were produced with the process parameters of No. 25 to obtain material specimens. The rotation angle of the electron beam for each layer was changed from 90° to 67° to eliminate anisotropy in the plane perpendicular to the building direction.

The as-built bars were then subjected to HIP and STA, the conditions of which are summarized in Table 3. Wrought UNS N07001 is subjected to a two-step aging process after solution treatment to precipitate the γ' phase and increase strength. The STA conditions for UNS N07001 built by EB-PBF were determined with reference to AMS5704L [32], which is the standard for wrought UNS N07001. Fig. 5 shows the equilibrium phase diagram of UNS N07001 calculated using Thermo-Calc. The calculations were performed using the TCNI12 database. The solvus temperature of the γ' phase of UNS N07001 is approximately 1030 °C. This indicates that the γ' phase, which precipitates during the AM process, is solubilized by HIP treatment at 1100 °C. In this study, three types of specimens were prepared, as listed in Table 3: "as-built" without heat treatment, "HIP" in which only HIP was conducted, and "HIP+STA" with both HIP and STA. Unocic et al. performed a solution treatment at 1135 °C for 10 min, followed by water quenching and a subsequent aging treatment with two steps (2 h at 1010 °C + 8 h at 788 °C), using Haynes 282 built by EB-PBF [28]. These heat treatment conditions were used considering standard heat treatments of wrought Haynes 282, where the temperatures were overall higher than those used for UNS N07001 in the present study.

The microstructure and precipitates in each as-built, HIP, and HIP+STA UNS N07001 specimen were evaluated. Field-emission SEM (FE-SEM; Hitachi High-Tech SU8700 and SU-70, Tokyo, Japan) and electron backscattered diffraction (EBSD; AMETEK Digi View, Pennsylvania, USA) were performed to evaluate the microstructure. Transmission electron microscopy (TEM; JEOL JEM-2100F and JEM-ARM200F Neoarm, Tokyo, Japan) was conducted to analyze precipitates.

Tensile test specimens were manufactured from 20 mm × 20 mm × 100 mm bars with the loading direction parallel to the building direction. Fig. 6 shows the geometry of a tensile test specimen. The number of test specimens was six per test temperature for the as-built specimens, whereas it was two per test temperature for the HIP and HIP+STA specimens. The test methods were performed in accordance with ASTM E8 and ASTM E21. The loading rate was 0.5 %/min up to the proof stress and 1.5 mm/min after reaching the proof stress. An extensometer with a gap of 10 mm between points was used, and the tensile

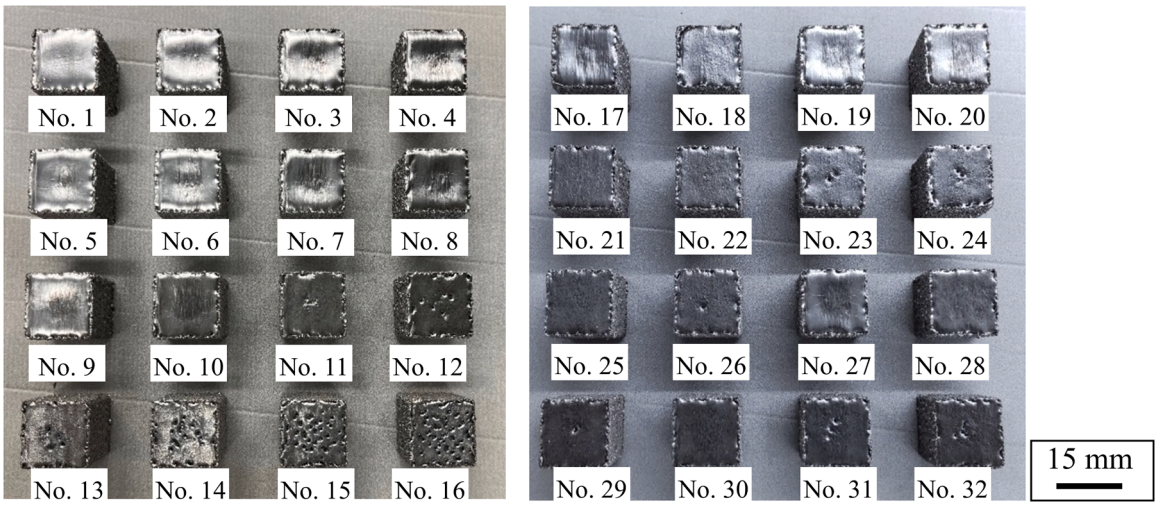

Fig. 4. Photographs of blocks produced using different parameters.

Table 3
Post-heat treatment conditions.

Specimen	HIP	STA
As-built	N/A	N/A
HIP	1100 °C / 147 MPa / 4 h	N/A
HIP+STA	1100 °C / 147 MPa / 4 h	1030 °C / 4 h / Ar gas cooling + 845 °C / 4 h / Ar gas cooling + 760 °C / 16 h / Air cooling

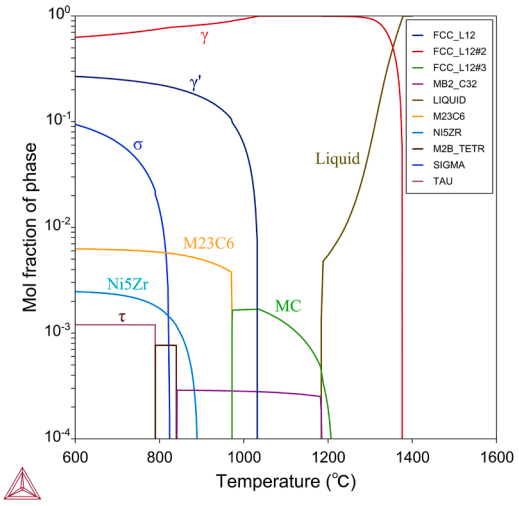

Fig. 5. Equilibrium phase diagram of UNS N07001 (Ni–20Cr–13.5Co–4.3Mo–0.03C–0.06Zr–0.005B–3Ti–1.5Al) obtained using Thermo-Calc software with the TCNI12 database.

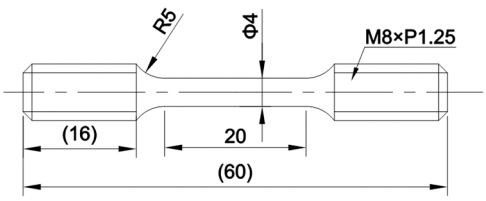

Fig. 6. Geometry of a tensile test specimen (mm).

tests were performed at RT and 538 °C. The mechanical properties at these temperatures are required in AMS5704L [32]. The fracture surface obtained after tensile testing was observed by SEM (JEOL JSM-6610, Tokyo, Japan).

3. Results and discussion

3.1. Effects of process parameters on surface morphology and hardness

Gui et al. [33] found that the internal state of a built part could be predicted from its surface morphology and two different surface roughness parameters. In the case of insufficient input energy, the surface becomes porous because of incomplete fusion. When the surface is porous, unmelted powder remains inside the printed part, resulting in irregular defects. In the case of appropriate input energy, the surface is flat, denoted by Gui and co-workers as "even." When the surface is even, there are no internal defects. In the case of excessive input energy, the surface becomes uneven. When the surface is uneven, spherical defects are generated inside the part.

In this study, the surface morphology of the 32 cubes (Table 2) was quantitatively evaluated with two surface roughness parameters: arithmetic mean height (*Sa*) and developed interfacial area ratio (*Sdr*) [34,35], referring to the work reported by Gui et al. [33]. *Sa* extends the arithmetic mean height (*Ra*) of a line to a surface. As shown in Eq. (1), *Sa* is the average of the difference in height of each point relative to the average height of the surface,

$$Sa = \frac{1}{A}\iint_A |Z(x,y)|dxdy. \quad (1)$$

Sdr expresses how much the surface area of the defined region is increased relative to the area of the defined region and can be expressed as shown in Eq. (2). *Sdr* is zero for a perfectly flat surface and increases with the slope of the surface.

$$Sdr = \frac{1}{A}\left[\iint_A \left(\sqrt{1+\left(\frac{\partial z(x,y)}{\partial x}\right)^2+\left(\frac{\partial z(x,y)}{\partial y}\right)^2}-1\right)dxdy\right], \quad (2)$$

where A is the defined area of the range to be measured, and $|z(x,y)|$ is the absolute value of the height of the average surface measured versus the height of convex deviations or depth of concave deviations.

The surface roughness and morphology of the 32 blocks are shown in Figs. 7 and 8, respectively. The color bar in Fig. 8 shows the height distribution when the average height of the measured surface was set to zero. The relative density values (ρ_r) of the 32 blocks are also shown in

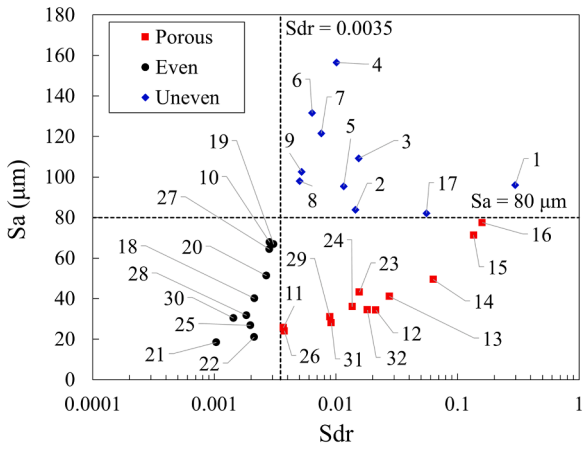

Fig. 7. Surface roughness of 32 blocks produced under different conditions designated by sample number.

Fig. 8. Fig. 9 depicts the relationship between the scanning speed and beam current used to construct the 32 blocks. Figs. 8 and 9 reveal that when the beam current was large and the scanning speed was low (i.e., the input energy density was high, and the surface of the block was uneven). These conditions caused *Sa* to increase, as shown in Fig. 7. In this study, when $Sa \geq 80$ μm, the surface was deemed uneven. When the beam current was small and the scanning speed was high (i.e., the input energy density was low, the surface of the block was not sufficiently melted), resulting in the large values of *Sdr*, as shown in Fig. 7. Based on the *Sdr* measurement results and surface morphology of the blocks, $Sa < 80$ μm and $Sdr \geq 0.0035$ were considered porous. For the other conditions, the input energy density was appropriate and the surface of the block was flat. If $Sa < 80$ μm and $Sdr < 0.0035$, the block was classified as even (i.e., neither uneven nor porous). Thus, the quantitative criteria for classifying the surface morphology of UNS N07001 blocks built by EB-PBF were defined as $Sa \geq 80$ μm: uneven, $Sa < 80$ μm and $Sdr \geq 0.0035$: porous, and $Sa < 80$ μm and $Sdr < 0.0035$: even. Although this evaluation method based on the study reported by Gui et al. [33] is simple, the process parameters that result in even surface morphology may be appropriate to produce UNS N07001 with desired properties. Fig. 8 shows that the blocks with porous surfaces (particularly Nos. 14, 15, and 16) had smaller relative densities. There was no significant difference in relative density between the blocks with uneven and even surfaces, but in some cases, blocks with uneven surfaces had a slightly higher relative density. Thus, it was difficult to determine the optimal process parameters based solely on the relative density, for UNS N07001 built by EB-PBF. As shown in Fig. 9, the range of process parameters that resulted in an even surface morphology was narrow. This is why the AM of UNS N07001 is difficult. Thus, the appropriate range of process parameters for EB-PBF of UNS N07001 was determined by examining 32 different combinations of beam current and scanning speed. Fig. 10 shows the Brinell hardness of the 32 blocks. The hardness of block No.

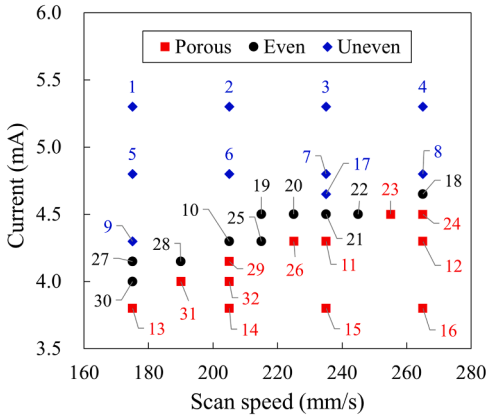

Fig. 9. Relationship between scanning speed and beam current used to construct 32 blocks, which are designated by sample number.

No.1	No.2	No.3	No.4	No.5	No.6	No.7	No.8
Uneven	Uneven	Uneven	Uneven	Uneven	Uneven	Uneven	Uneven
$\rho_r = 0.9979$	$\rho_r = 0.9974$	$\rho_r = 0.9979$	$\rho_r = 0.9971$	$\rho_r = 0.9956$	$\rho_r = 0.9966$	$\rho_r = 0.9963$	$\rho_r = 0.9957$
No.9	**No.10**	**No.11**	**No.12**	**No.13**	**No.14**	**No.15**	**No.16**
Uneven	Even	Porous	Porous	Porous	Porous	Porous	Porous
$\rho_r = 0.9945$	$\rho_r = 0.9941$	$\rho_r = 0.9923$	$\rho_r = 0.9883$	$\rho_r = 0.9880$	$\rho_r = 0.9756$	$\rho_r = 0.9632$	$\rho_r = 0.9493$
No.17	**No.18**	**No.19**	**No.20**	**No.21**	**No.22**	**No.23**	**No.24**
Uneven	Even	Even	Even	Even	Even	Porous	Porous
$\rho_r = 0.9951$	$\rho_r = 0.9946$	$\rho_r = 0.9945$	$\rho_r = 0.9941$	$\rho_r = 0.9943$	$\rho_r = 0.9943$	$\rho_r = 0.9932$	$\rho_r = 0.9934$
No.25	**No.26**	**No.27**	**No.28**	**No.29**	**No.30**	**No.31**	**No.32**
Even	Porous	Even	Even	Porous	Even	Porous	Porous
$\rho_r = 0.9943$	$\rho_r = 0.9930$	$\rho_r = 0.9938$	$\rho_r = 0.9932$	$\rho_r = 0.9929$	$\rho_r = 0.9939$	$\rho_r = 0.9932$	$\rho_r = 0.9913$

Fig. 8. Three-dimensional surface topographical images and relative density of 32 blocks produced under different conditions.

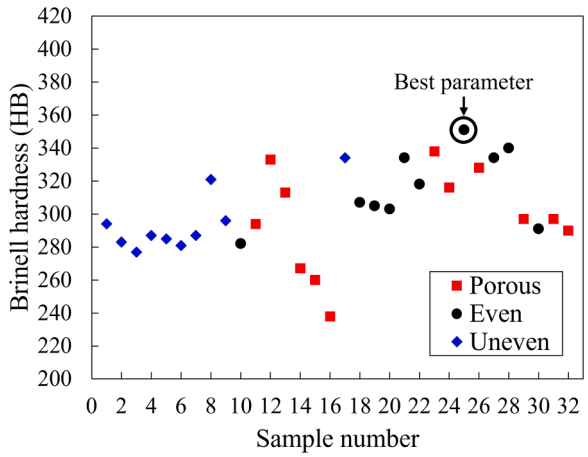

Fig. 10. Brinell hardness of blocks produced using different parameters.

25 (scan speed = 215 mm/s, current = 4.30 mA) was the highest among the specimens. Overall, the parameters used to produce No. 25 were determined to be the optimal parameters because they provided both an even surface and the highest Brinell hardness. The layer thickness, line offset, and preheat temperature used for No. 25 were almost the same as those used for the Haynes 282 developed by Singh et al. [29], but the current was smaller and the scan speed was slower for No. 25.

3.2. Microstructure of UNS N07001 built by EB-PBF

To evaluate the effect of post-heat treatment on the microstructure of UNS N07001 built with No. 25 process parameters, the microstructure was observed by EBSD and FE-SEM, and precipitates were analyzed by TEM. Figs. 11 and 12 show EBSD inverse pole figure maps and back-scattered electron images of UNS N07001 built by EB-PBF, respectively. The cross-section parallel to the building direction was observed. Fig. 11 reveals that UNS N07001 built by EB-PBF possessed a columnar crystal structure that grew along the printing direction regardless of post-heat treatment conditions. Post-heat treatment did not change the grain size of the specimens. Fig. 12(a) and (b) shows that cracks were present at grain boundaries and the grains contained pores in the as-built specimen. In contrast, no cracks were observed in the HIP and HIP+-STA specimens (Fig. 12(c) and (e)). Thus, the cracks were removed by HIP at high temperature and pressure. Fig. 12(f) reveals that the HIP+STA specimen contained continuous fine precipitates at the grain boundaries, unlike the as-built and HIP specimens.

Figs. 13–15 depict bright-field TEM images and energy-dispersive X-ray spectroscopy (EDS) mapping results for the specimens, which were obtained to allow a more detailed evaluation of precipitates. Precipitates identified by TEM electron diffraction are shown in the bright-field image. The as-built specimen (Fig. 13) contained MX-type precipitates (including Ti(C, N) and some Mo) with sizes of 200–500 nm at the grain boundary and within the grain. A plate-like γ' phase ($Ni_3(Ti, Al)$) with a width of ~500 nm and a length of several micrometers was observed at the grain boundary. A grain-like γ' phase with a size of approximately 100–200 nm and a partly coarse octodendritic γ' phase with a size of approximately 1–2 μm were distributed within the grain (Fig. 13). Fig. 14 reveals that neither the plate-like γ' phase at grain boundaries nor the coarse γ' phase with a size of 1–2 μm within the grains, detected in the as-built specimen, remained in the HIP specimen. These precipitates were presumably eliminated by HIP treatment. Instead, MX-type precipitates with sizes of 100–800 nm were observed at the grain boundaries and within the grains, and grain-like γ' phase particles with sizes of 100–150 nm were observed within the grains. The HIP+STA specimen (Fig. 15) contained MX-type precipitates with sizes of 100–400 nm at grain boundaries and $M_{23}C_6$-type precipitates (M = Cr > Fe) with sizes of 100–300 nm at grain boundaries within grains. A grain-like γ' phase with a size of 50 nm and a partially grain-like γ' phase with a size of ~300 nm were distributed in the grains. Haynes 282 built by EB-PBF [29] also contained TiC within the grain and at the grain boundary. In addition, grain-like γ' phase particles with sizes of 50–110 nm were observed within the grains, similar to the UNS N07001 built by EB-PBF in this study. However, unlike UNS N07001, a plate-like γ' phase was not observed at the grain boundary.

Fig. 16 shows dark-field images collected using the < 100 > superlattice reflection in the γ' phase within the grains. Fig. 16 (a) illustrates that a γ' phase with a particle size of 100–200 nm precipitated in the as-built specimen. In EB-PBF, the powder is pre-heated before the melting and solidification processes of each layer to prevent smoke formation. Therefore, the specimen is kept at a high temperature of several hundred degrees Celsius during the construction process. This suggests that the γ' phase, which is a precipitation strengthening phase, precipitated even in the as-built specimen because of its long exposure to the γ'-phase precipitation temperature range of UNS N07001. Additionally, the γ' phase precipitates in the as-built Haynes 282 specimens built by EB-PBF for the same reason [29]. Fig. 16(b) shows that γ'-phase particles with a size of 100–150 nm

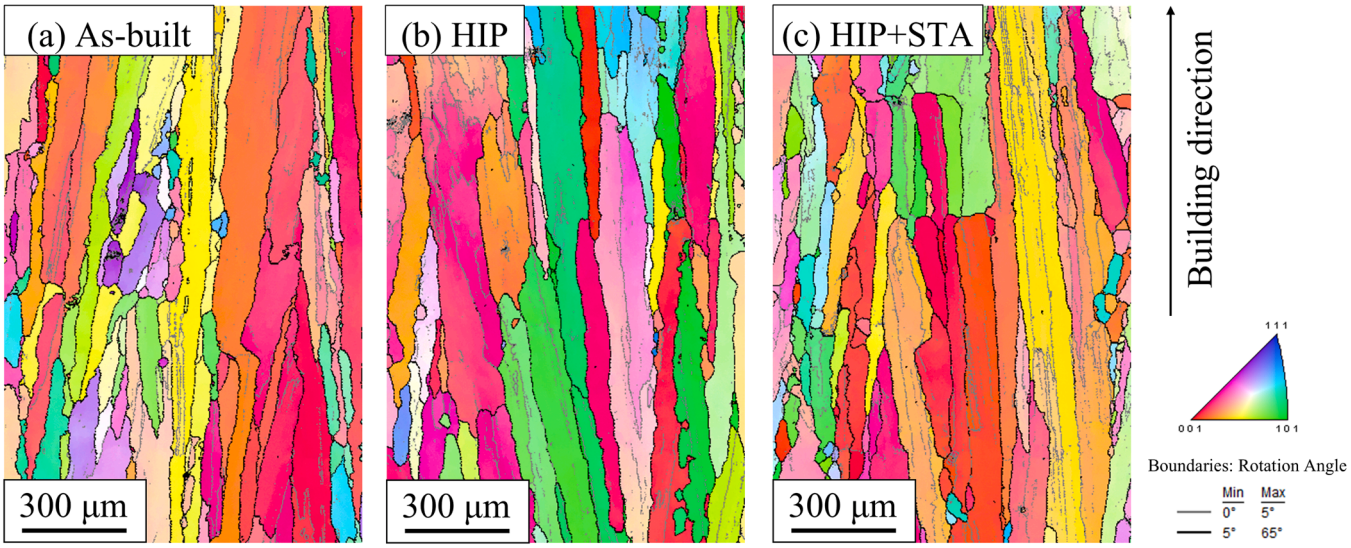

Fig. 11. EBSD inverse pole figure maps of UNS N07001 built by EB-PBF. (a) As-built, (b) HIP, and (c) HIP+STA.

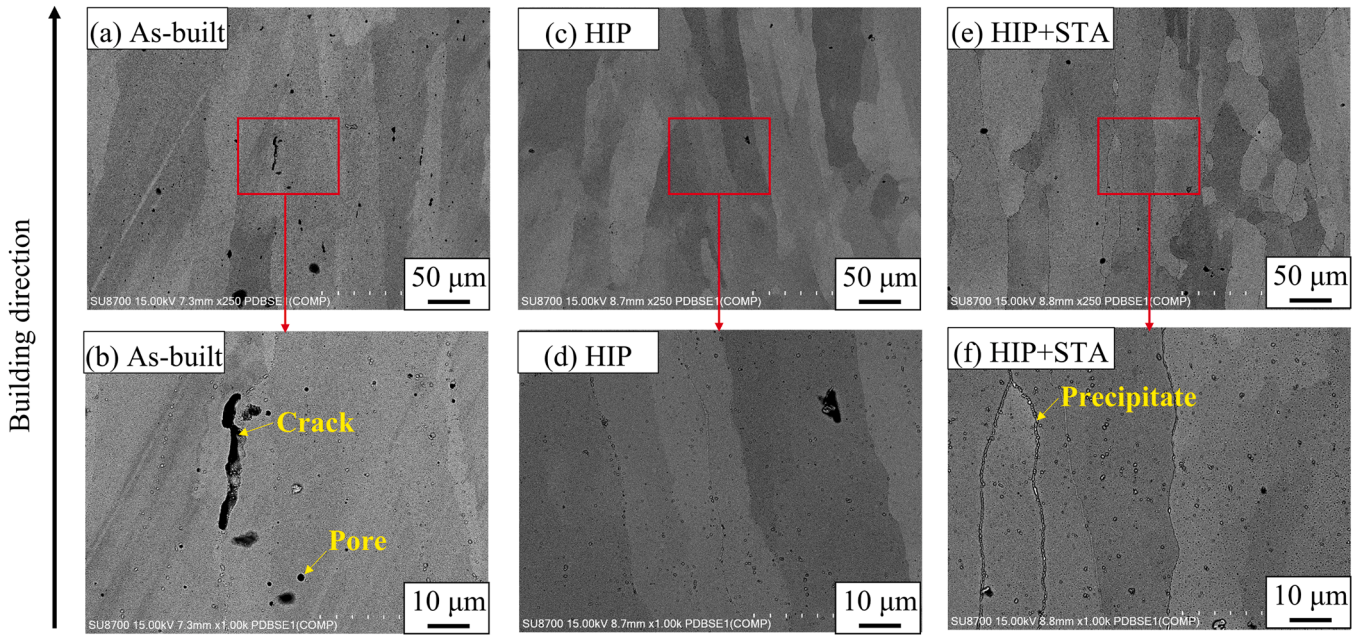

Fig. 12. BSE images of UNS N07001 built by EB-PBF. (a), (b) As-built, (c), (d) HIP, and (e), (f) HIP+STA specimens.

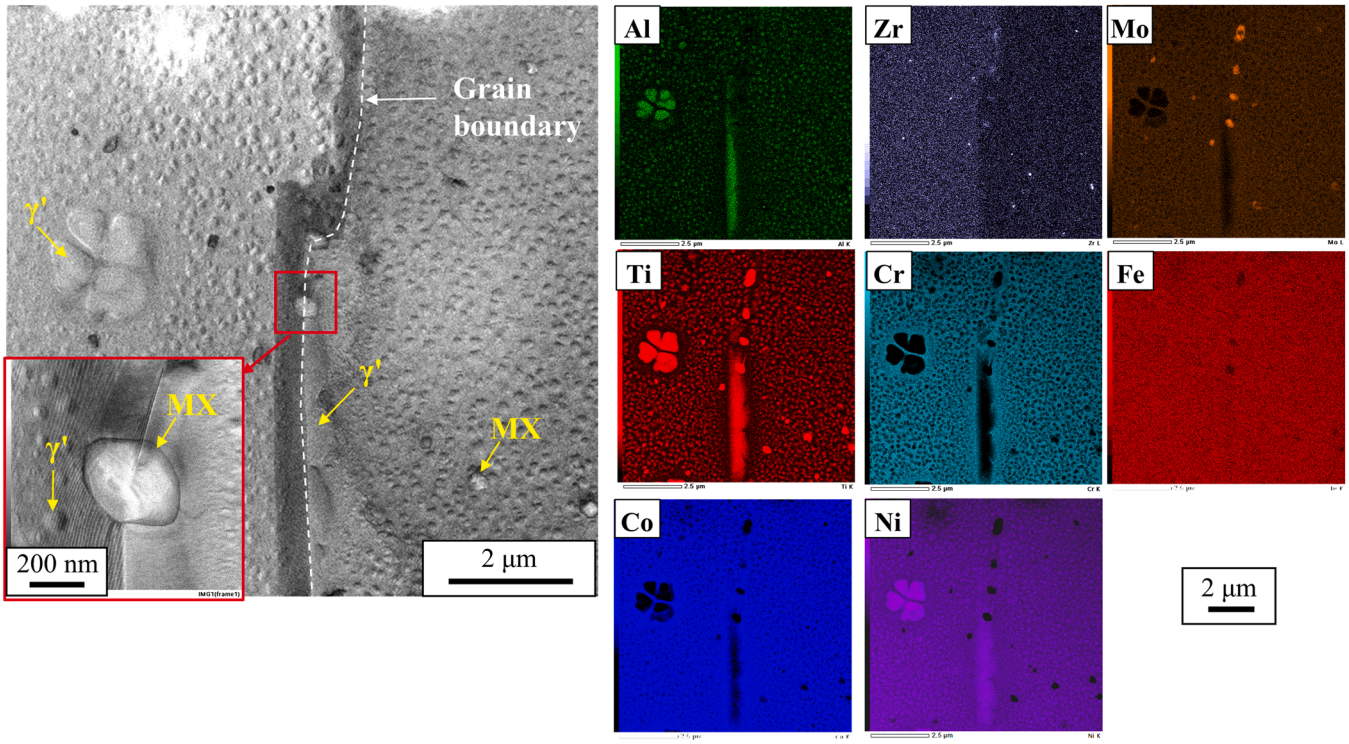

Fig. 13. TEM bright-field micrographs and corresponding EDS mapping of the as-built UNS N07001 specimen.

precipitated in the HIP specimen. The γ' phase observed in the as-built specimen may dissolve during HIP, which is performed at a higher temperature (1100 °C) than the solvus temperature of the γ' phase. However, the cooling rate of the HIP process is slow, which may lead to the precipitation of the γ' phase during the cooling process. γ'-phase particles with sizes of approximately 50 and 300 nm precipitated together in the HIP+STA specimen (Fig. 16(c)). The γ' particles with a size of ~300 nm may be the primary γ' phase, and the smaller particles may be the secondary γ' phase. Fig. 17 shows EDS mapping images of Ti, revealing that the area fraction of the γ' phase was much higher in the HIP+STA specimen than in the as-built and HIP specimens. This indicates that HIP and STA increased the amount of fine γ' phase.

3.3. Tensile test results

To evaluate the effect of post-heat treatment on the mechanical properties of UNS N07001 built by EB-PBF, tensile tests were performed. Table 4 lists the tensile test results at RT and 538 °C for the as-built, HIP, and HIP+STA specimens. Fig. 18 presents the stress-displacement curves for the specimens. The HIP specimen showed slight improvements of

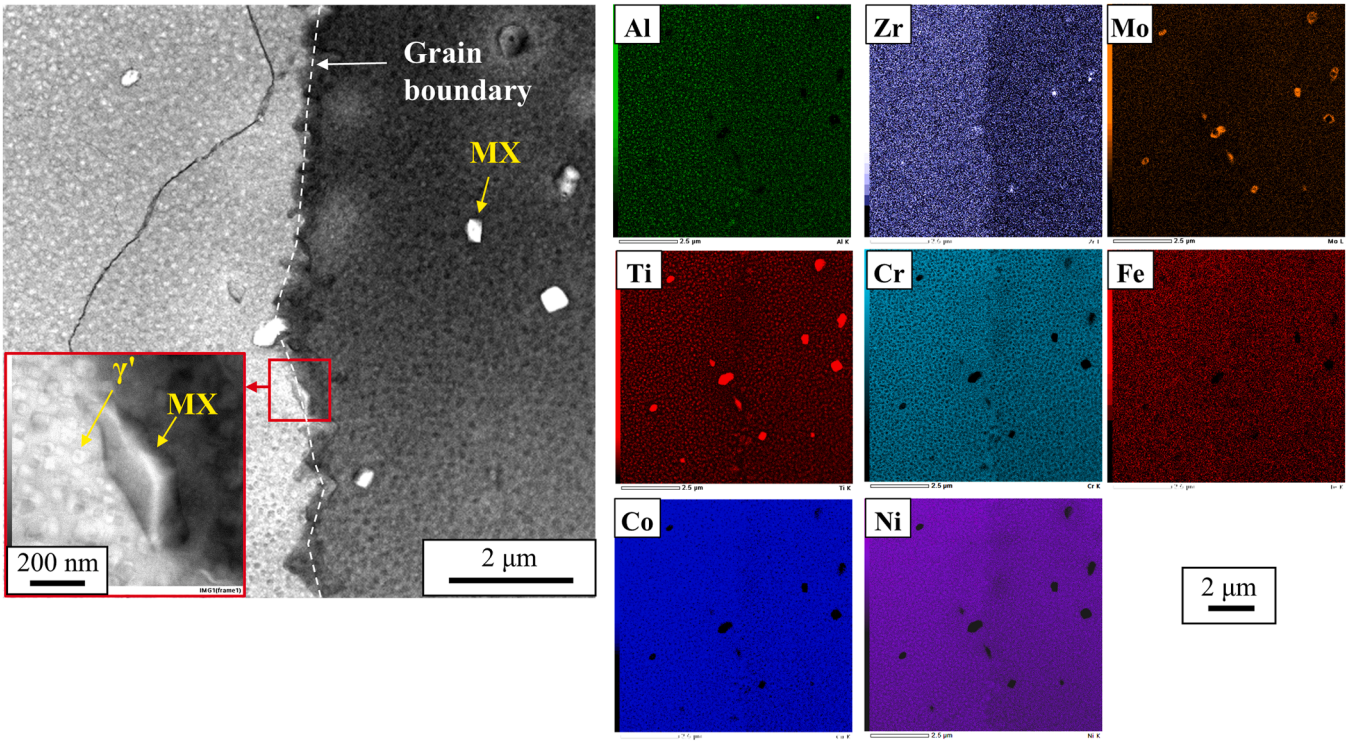

Fig. 14. TEM bright-field micrographs and corresponding EDS mapping of the UNS N07001 specimen after HIP.

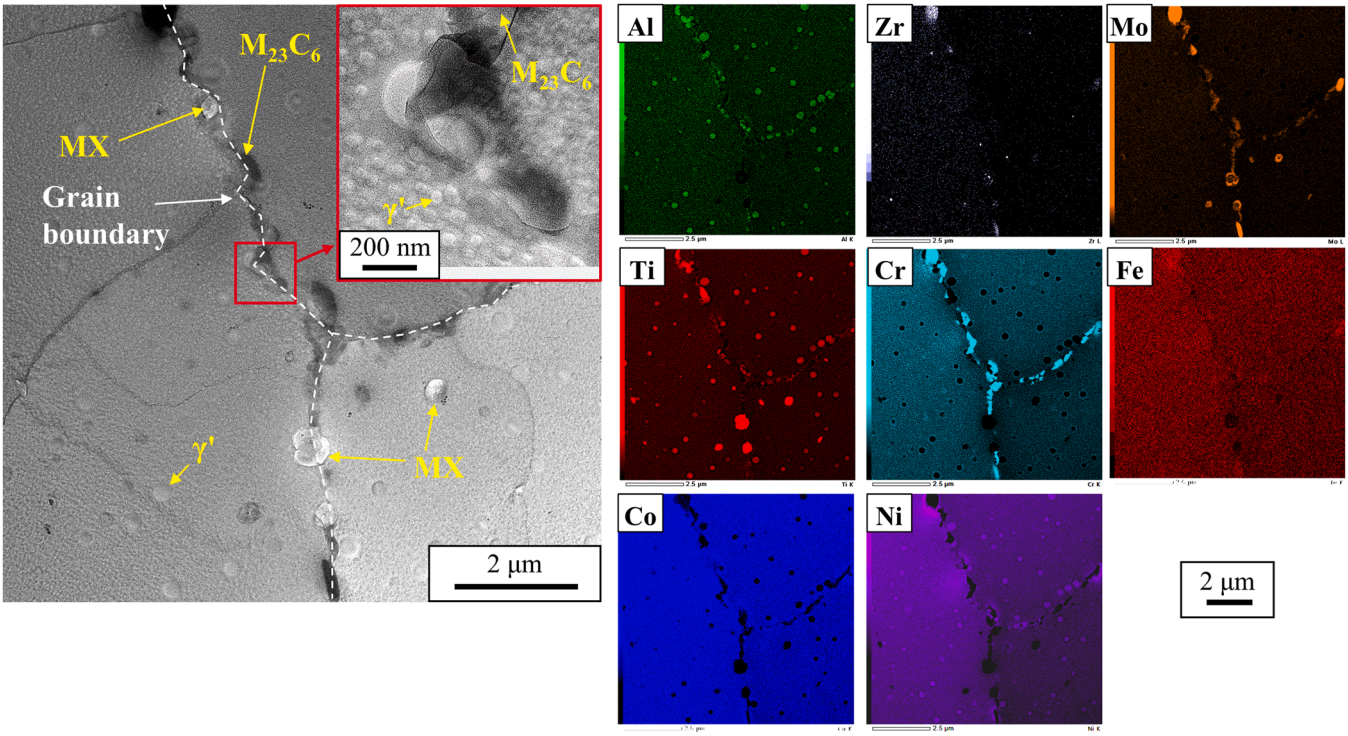

Fig. 15. TEM bright-field micrographs and corresponding EDS mapping of the UNS N07001 specimen after HIP and STA treatment.

both 0.2 % proof stress and tensile strength and similar ductility to those of the as-built specimen. These changes are attributed to HIP removing defects such as cracks and pores (Fig. 12). The 0.2 % proof stress and tensile strength of the HIP+STA specimen were much higher than those of the as-built and HIP specimens. This may be attributed to the higher content of fine γ' precipitates in the HIP+STA specimen compared with that in the other specimens (Figs. 16 and 17). Murugan et al. evaluated the precipitation strengthening mechanism of wrought UNS N07001 by employing micro-indentation experiments and theoretical models and revealed that shearing by weakly coupled dislocations was dominant for samples with a γ' particle size (r_p) lower than 18 nm, shearing by strongly coupled dislocations was dominant for samples with a r_p range

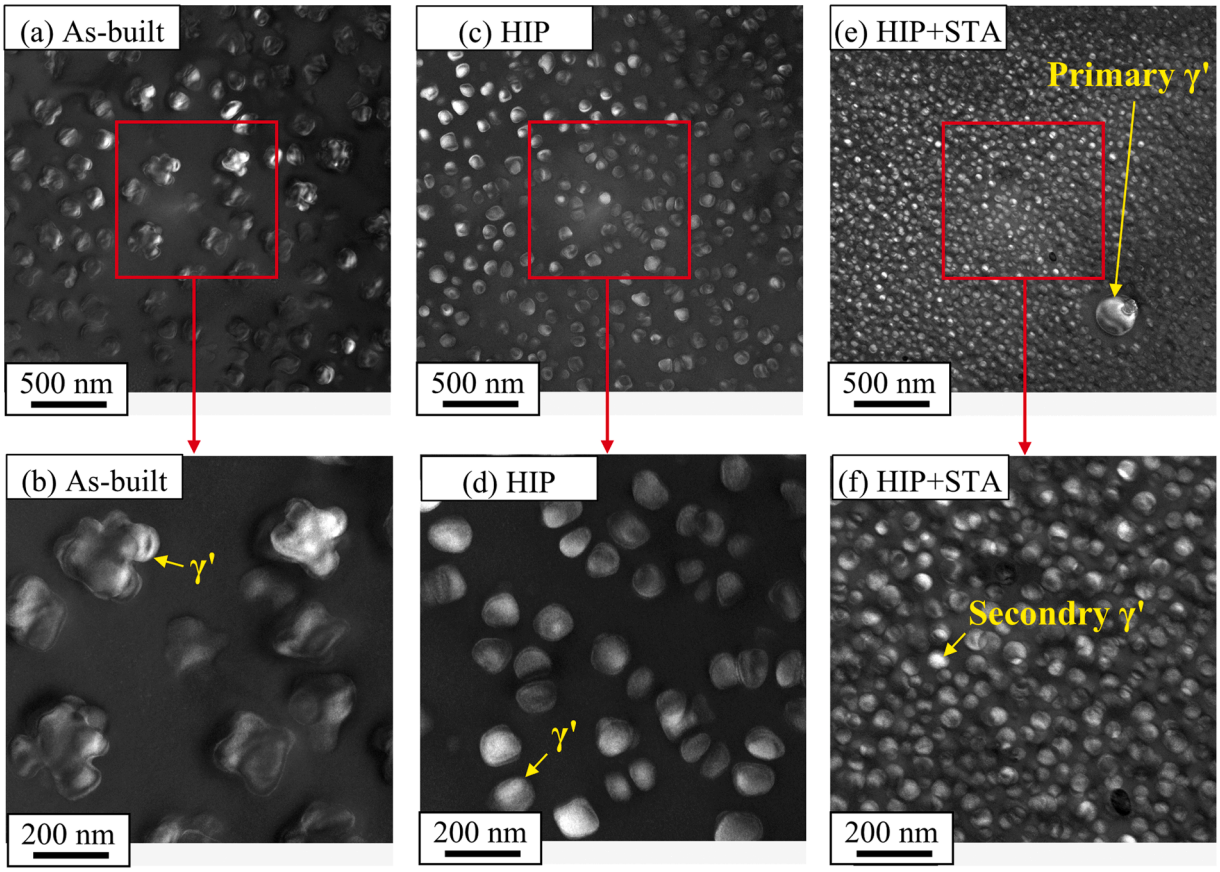

Fig. 16. TEM dark-field micrographs collected using the < 100 > superlattice reflection of the γ′ phase for the (a), (b) as-built, (c), (d) HIP, and (e), (f) HIP+-STA specimens.

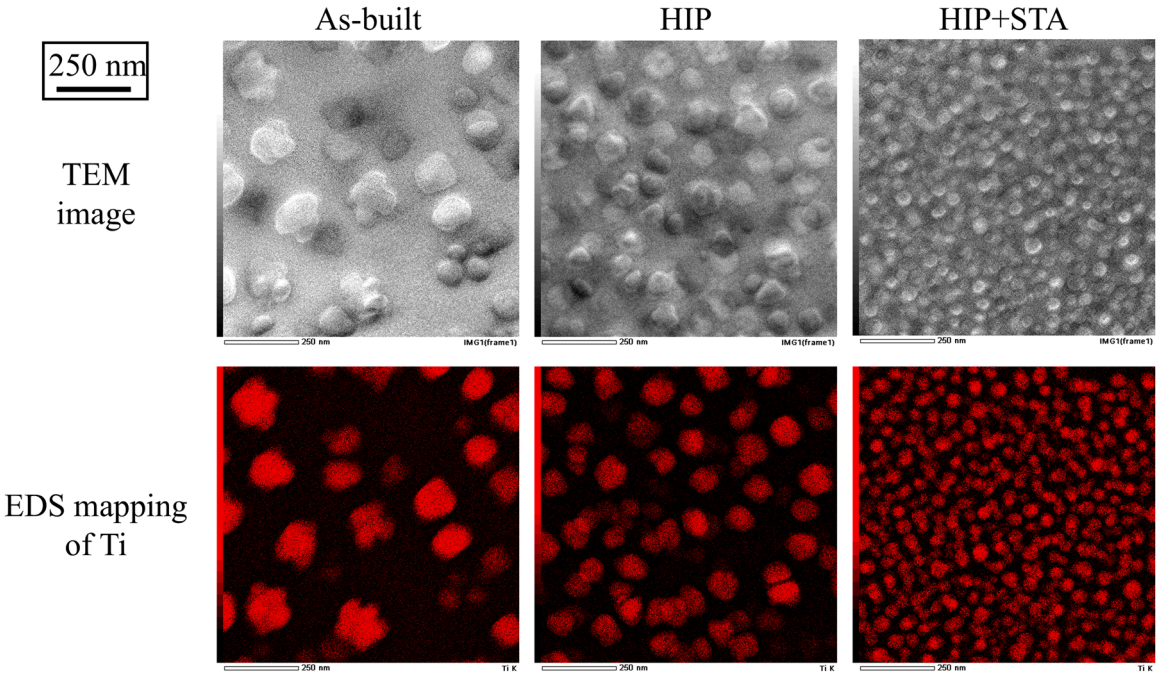

Fig. 17. TEM images and EDS mapping images of Ti for the as-built, HIP, and HIP+STA specimens.

of 18–98 nm, and Orowan bypassing was dominant for samples with a r_p larger than 98 nm [36]. Given that the γ' particle size in the HIP+STA specimen in this study is approximately 50 nm, the precipitation strengthening mechanism may be dominated by strongly coupled dislocations, which contributes the increase of 0.2 % proof stress.

Fig. 19 shows the mechanical properties of UNS N07001 built by EB-

Table 4
Tensile test results for UNS N07001 specimens built by EB-PBF.

Test temperature	Heat treatment condition	Tensile stress (MPa)	0.2 % proof stress (MPa)	Elongation (%)	Reduction of area (%)	Young's modulus (GPa)
RT	As-built	1049	546	28	37	136
	HIP	1062	608	30	42	136
	HIP+STA	1203	784	26	38	149
538 °C (1000 °F)	As-built	889	472	23	27	117
	HIP	895	530	26	32	119
	HIP+STA	1008	675	20	28	125

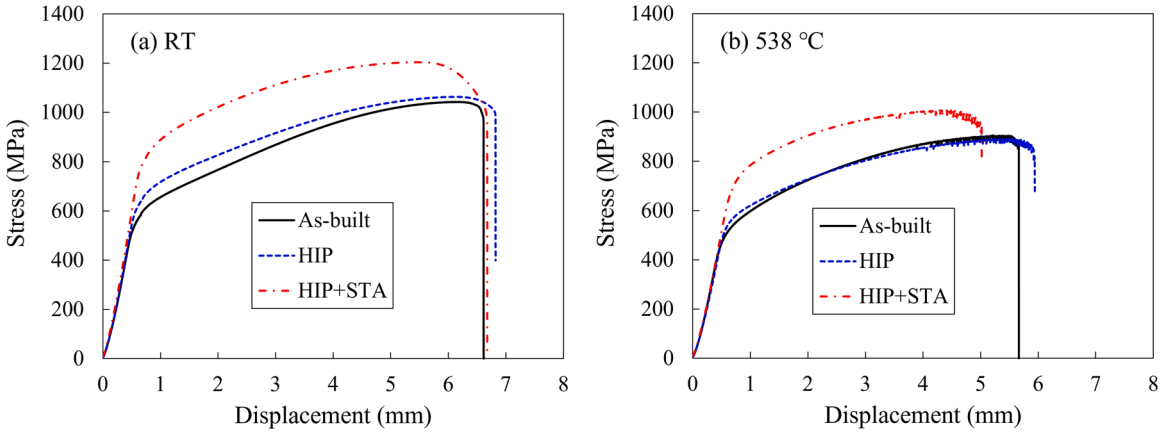

Fig. 18. Stress-displacement curve of UNS N07001 specimens built by EB-PBF at (a) RT and (b) 538 °C.

PBF normalized by those of AMS5704L requirements [32]. At RT (Fig. 19(a)), the elongation and the area reduction greatly exceeded the AMS5704L requirements, regardless of the heat treatment conditions. The tensile strength and 0.2 % proof stress of the as-built and HIP specimens were below AMS5704L requirements, whereas those of the HIP+STA specimen were comparable to the AMS5704L requirements. Fig. 19(b) shows the mechanical properties of the specimens measured at 538 °C. The results showed a similar trend to those at RT, that is, the elongation and the reduction of area exceeded the AMS5704L requirements regardless of the heat treatment conditions. The tensile strength and 0.2 % proof stress of the as-built and HIP specimens were below AMS5704L requirements, whereas those of the HIP+STA specimen were almost equal to AMS5704L requirements. Thus, STA after HIP treatment markedly improved the mechanical properties of UNS N07001 built by EB-PBF to a level comparable to the requirements of the wrought material.

Figs. 20 and 21 show representative SEM images of fracture surfaces after tensile testing at RT and 538 °C, respectively. Fig. 20(a) shows that several vertical cracks were present on the fracture surface of the as-built specimen. The number of cracks was higher than that before tensile testing (Fig. 12(a) and (b)). It is considered that the internal cracks coalesced or grew during tensile testing. Fig. 20(b) and (c) presents magnified views of the fracture surface in a crack-free region and near cracks, respectively. In both images, dimples of approximately 5 μm were uniformly distributed, indicating that ductile fracture was the dominant failure mechanism in the as-built specimen at RT. Fig. 20(d) displays the fracture surface of the HIP specimen, which has no cracks. Fig. 20(e) and (f) reveals that dimples were present over the entire fracture surface, indicating that ductile fracture occurred in the HIP specimen. The HIP treatment removed cracks and pores from the HIP specimen (Fig. 12(c) and (d)), which resulted in a crack-free fracture surface, unlike the case for the as-built specimen. The fracture surface of

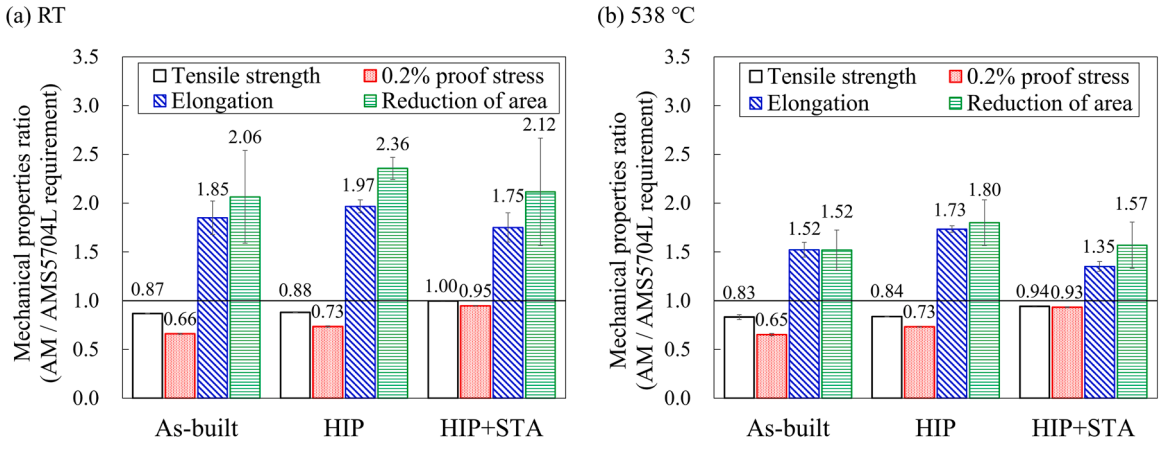

Fig. 19. Mechanical properties ratio (AM/AMS5704L requirement) of UNS N07001 specimens at (a) RT and (b) 538 °C.

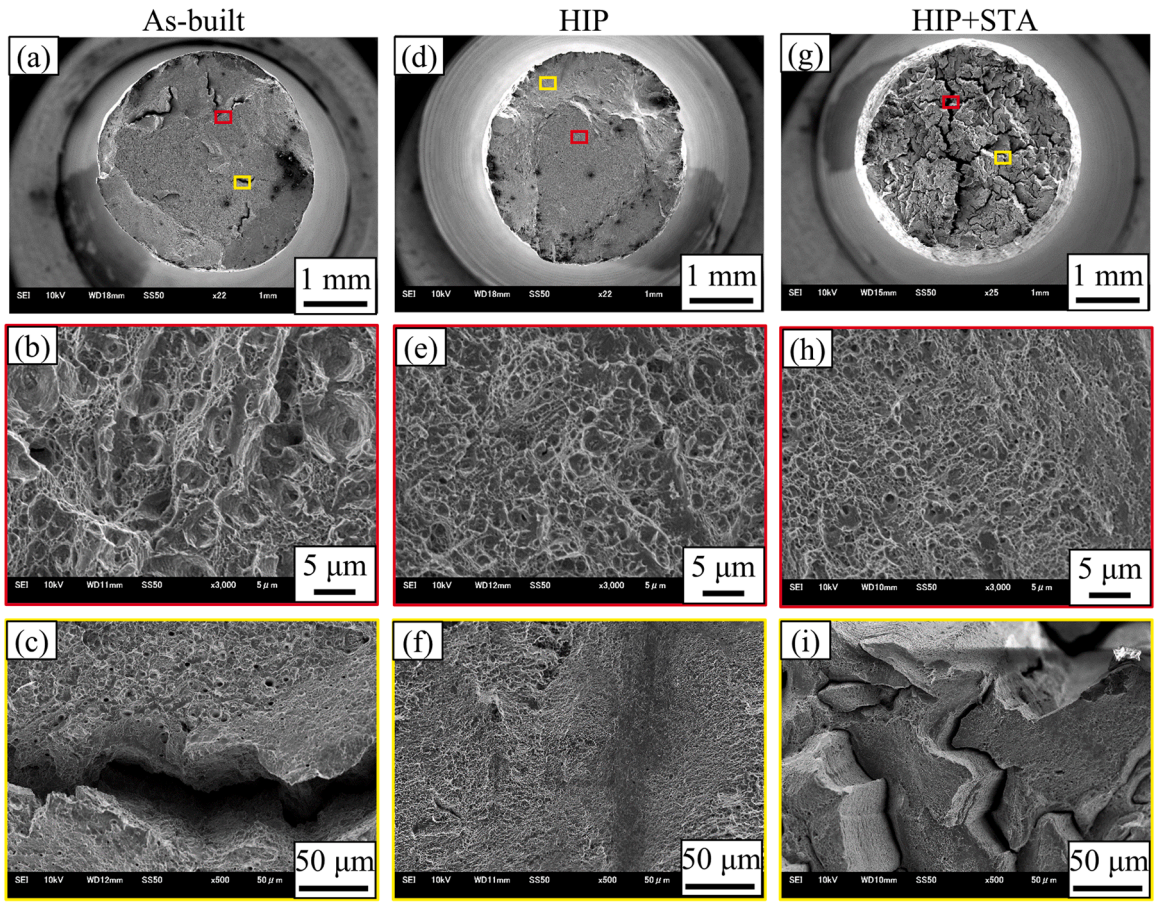

Fig. 20. SEM images of fracture surfaces after tensile testing at RT. (a–c) As-built, (d–f) HIP, and (g–i) HIP+STA specimens.

the HIP+STA specimen contained many vertical cracks parallel to the loading direction (Fig. 20(g)), similar to the as-built specimen. Because these cracks were not observed before tensile testing (Fig. 12(e) and (f)), they likely formed during the tensile test. Fig. 20(h) shows that dimples were present in the crack-free region, whereas few dimples were observed near the cracks (Fig. 20(i)). It suggests that the fracture surface in the crack-free region may be ductile, whereas that near cracks may be brittle. Fig. 15 reveals that $M_{23}C_6$-type precipitates (M = Cr > Fe) with a size of 100–300 nm were present at the grain boundaries of the HIP+-STA specimen before tensile testing. It is speculated that the $M_{23}C_6$ precipitates made the grain boundaries brittle, promoting crack formation at the grain boundaries during tensile testing.

Fig. 21 shows the fracture surface of the specimens after tensile testing at 538 °C. The overall behavior was similar to that at RT. Cracks were observed in the fracture surface of the as-built and HIP+STA specimens, whereas no cracks were observed for the HIP specimen. The reasons for this would be the same as those at RT. However, fewer cracks were observed in the HIP+STA specimen at 538 °C than at RT. This may be because the $M_{23}C_6$ precipitates, which induce the brittle cracking along grain boundaries, become relatively ductile at higher temperatures.

In summary, the STA performed in this study increased the strength of UNS N07001 built by EB-PBF by promoting the precipitation of the γ' phase, but simultaneously generated $M_{23}C_6$-type precipitates, which induced vertical cracking along the grain boundaries during tensile testing. Even though the vertical cracks parallel to the loading direction did not strongly affect the 0.2 % proof stress and tensile strength, the precipitation of $M_{23}C_6$ should be suppressed to improve reliability. Note that vertical cracks may lead to a critical reduction in strength against loading from the transverse direction. The mechanical properties of the HIP+STA specimen could be further improved by optimizing heat treatment conditions to prevent crack formation by suppressing precipitation of $M_{23}C_6$ at grain boundaries during STA.

4. Conclusion

The process parameters of EB-PBF for the γ' precipitate-strengthened Ni-based superalloy UNS N07001 were optimized by evaluating the surface roughness and Brinell hardness of blocks built with 32 different process parameters. Specimens built with the optimal parameters were subjected to post-heat treatment. Microstructure observation, precipitate analysis, and tensile tests were performed to examine the effects of post-heat treatment on the microstructure and mechanical properties of UNS N07001 printed by EB-PBF. In addition, fracture surfaces were observed after tensile testing to investigate the fracture mechanism. The following findings were obtained.

1. An appropriate combination of EB-PBF process parameters was determined for UNS N07001 by examining 32 different beam currents and scanning speeds. A scan speed of 215 mm/s and current of 4.30 mA were determined to be optimal because they enabled the highest Brinell hardness and an even surface.
2. UNS N07001 built by EB-PBF consisted of columnar crystals that grew along the building direction. The as-built specimen contained small cracks and pores with MX-type precipitates and γ' phase at grain boundaries and within grains. Cracks and pores disappeared from the HIP specimen and it contained MX-type precipitates at the grain boundaries and inside the grains and γ' phase inside the grains. The HIP+STA specimen contained MX-type precipitates at the grain boundaries and within the grains, $M_{23}C_6$-type precipitates at the

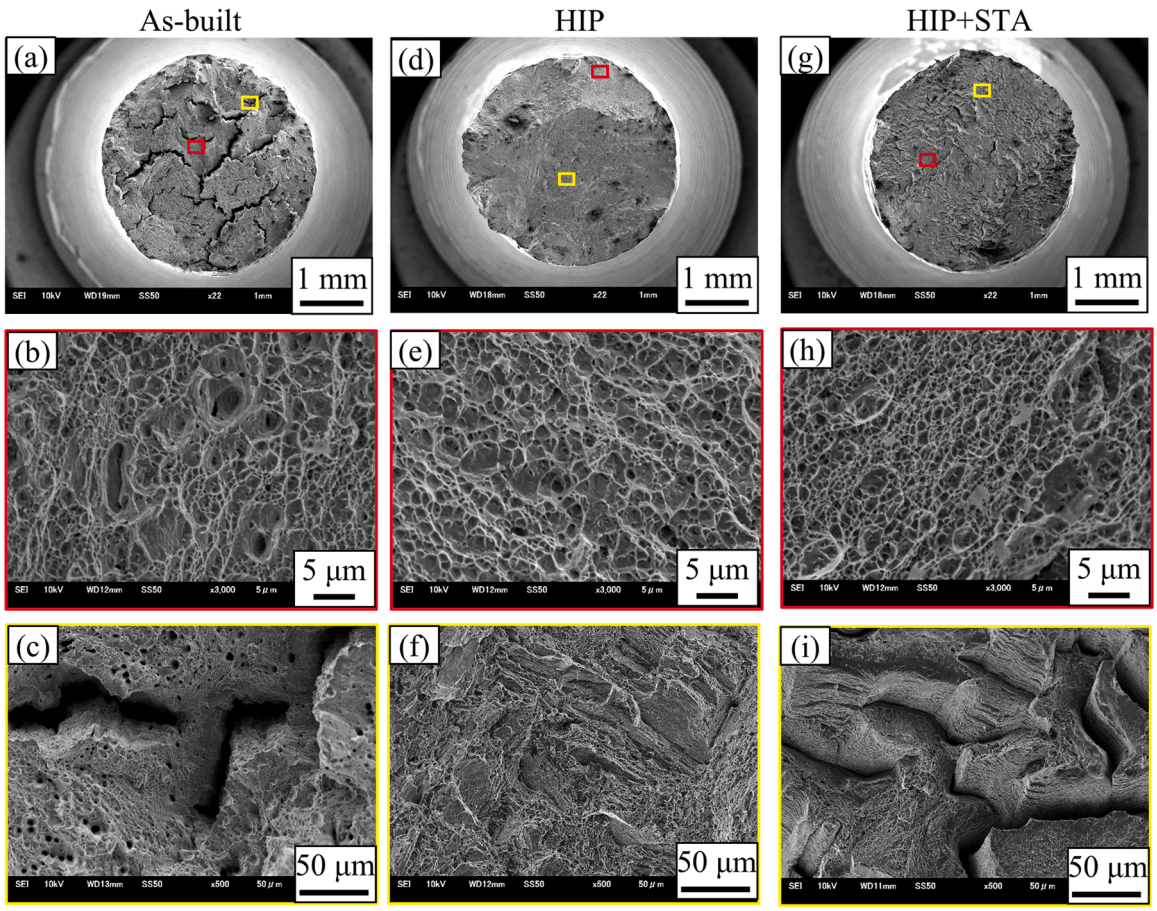

Fig. 21. SEM images of fracture surfaces after tensile testing at 538 °C. (a–c) As-built, (d–f) HIP, and (g–i) HIP+STA specimens.

grain boundaries, and γ' phase within the grains. Compared with the as-built and HIP specimens, the HIP+STA specimen contained a higher content of fine γ' phase.

3. HIP treatment alone had little effect on the mechanical properties of UNS N07001 built by EB-PBF. In contrast, STA after HIP treatment markedly improved the mechanical properties to a level comparable to the requirements for the wrought material. The HIP+STA specimen was equivalent to that of the as-built specimen, which may be caused by the former containing a larger amount of fine γ' precipitates than the other specimens.
4. Cracks were observed on the fracture surface of the as-built specimen after tensile testing. It is considered that existing cracks grew during tensile testing. No cracks were observed on the fracture surface of the HIP specimen, suggesting that cracks did not develop during tensile testing. Many cracks were observed on the fracture surface of the HIP+STA specimen. The $M_{23}C_6$-type precipitates present at the grain boundaries before tensile testing made the grain boundaries brittle, which led to crack formation at the grain boundaries during tensile testing.

CRediT authorship contribution statement

Takakuwa Ryo: Writing - Original Draft, Conceptualization, Methodology, Formal analysis, Investigation, Visualization. **Sakaguchi Motoki:** Writing - review & editing, Visualization, Supervision. **Chin Yuante:** Investigation, Methodology. **Nakamoto Hiroaki:** Writing – review & editing. **Noguchi Manabu:** Project administration. **Inoue Hirotsugu:** Supervision.

Declaration of Competing Interest

The authors declare that they have no known competing financial interests or personal relationships that could have appeared to influence the work reported in this paper.

Acknowledgment

We thank Natasha Lundin, PhD, and Robert Ireland, PhD, from Edanz (https://jp.edanz.com/ac) for editing a draft of this manuscript.

Data Availability

Data will be made available on request.

References

[1] ASTM Standard F2792-12a, Standard terminology for additive manufacturing technologies, (2009).
[2] C. Korner, Additive manufacturing of metallic components by selective electron beam melting - a review, Int. Mater. Rev. 61 (2016) 361–377, https://doi.org/10.1080/09506608.2016.1176289.
[3] J.N. Dupont, J.C. Lippold, S.D. Kiser, Welding Metallurgy and Weldability of Nickel Base Alloys, Wiley, 2009, https://doi.org/10.1002/9780470500262.
[4] Y. Nakao, K. Mitsuhata, Reheat cracking phenomena in Ni-base superalloy Waspaloy, Q. J. JWS 3 (4) (1985) 808–815, https://doi.org/10.2207/qjjws.3.808.
[5] A.T.D.'Annessa, Procedures for avoiding heat-treat cracking in nickel-base superalloy weldments, Tech. Report AFML-TR-72-17 (1972).
[6] M. Qian, J.C. Lippold, The effect of annealing twin-generated special grain boundaries on HAZ liquation cracking of nickel-base superalloys, Acta Mater. 51 (2003) 3351–3361, https://doi.org/10.1016/S1359-6454(03)00090-9.
[7] H.E. Helmer, C. Korner, R.F. Singer, Additive manufacturing of nickel-based superalloy Inconel 718 by selective electron beam melting: Processing window and

microstructure, J. Mater. Res. 29 (2014) 1987–1996, https://doi.org/10.1557/jmr.2014.192.
[8] H.E. Helmer, A. Bauerei, R.F. Singer, C. Korner, Grain structure evolution in Inconel 718 during selective electron beam melting, Mater. Sci. Eng. A 668 (2016) 180–187, https://doi.org/10.1016/j.msea.2016.05.046.
[9] N. Raghavan, R. Dehoff, S. Pannala, S. Simunovic, M. Kirka, J. Turner, N. Carlson, S.S. Babu, Numerical modeling of heat-transfer and the influence of process parameters on tailoring the grain morphology of IN718 in electron beam additive manufacturing, Acta Mater. 112 (2016) 303–314, https://doi.org/10.1016/j.actamat.2016.03.063.
[10] M.M. Kirka, K.A. Unocic, N. Raghavan, F. Medina, R.R. Dehoff, S.S. Babu, Microstructure development in electron beam-melted Inconel 718 and associated tensile properties, JOM 68 (2016) 1012–1020, https://doi.org/10.1007/s11837-016-1812-6.
[11] M.M. Kirka, F. Medina, R. Dehoff, A. Okello, Mechanical behavior of post-processed Inconel 718 manufactured through the electron beam melting process, Mater. Sci. Eng. A 680 (2017) 338–346, https://doi.org/10.1016/j.msea.2016.10.069.
[12] D. Deng, J. Moverare, R.L. Peng, H. Söderberg, Microstructure and anisotropic mechanical properties of EBM manufactured Inconel 718 and effects of post heat treatments, Mater. Sci. Eng. A 693 (2017) 151–163, https://doi.org/10.1016/j.msea.2017.03.085.
[13] S. Goel, E. Zaninelli, T. Gundgire, M. Ahlfors, O. Ojo, U. Klement, S. Joshi, Microstructure evolution and mechanical response-based shortening of thermal post-treatment for electron beam melting (EBM) produced Alloy 718, Mater. Sci. Eng. A 820 (2021) 141515, https://doi.org/10.1016/j.msea.2021.141515.
[14] Y.L. Kuo, A. Kamigaichi, K. Kakehi, Characterization of Ni-based superalloy built by selective laser melting and electron beam melting, Metall. Mater. Trans. A 49A (2018) 3831–3837, https://doi.org/10.1007/s11661-018-4769-y.
[15] Y.L. Kuo, S. Horikawa, K. Kakehi, Effects of build direction and heat treatment on creep properties of Ni-base superalloy built up by additive manufacturing, Scr. Mater. 129 (2017) 74–78, https://doi.org/10.1016/j.scriptamat.2016.10.035.
[16] Y.L. Kuo, T. Nagahari, K. Kakehi, The effect of post-processes on the microstructure and creep properties of Alloy718 built up by selective laser melting, Materials 11 (2018) 996, https://doi.org/10.3390/ma11060996.
[17] A.R. Balachandramurthi, J. Moverare, S. Mahade, R. Pederson, Additive manufacturing of Alloy 718 via electron beam melting: effect of post-treatment on the microstructure and the mechanical properties, Materials 12 (2019) 68, https://doi.org/10.3390/ma12010068.
[18] A.R. Balachandramurthi, J. Moverarea, N. Dixit, R. Pederson, Influence of defects and as-built surface roughness on fatigue properties of additively manufactured Alloy 718, Mater. Sci. Eng. A 735 (2018) 463–474, https://doi.org/10.1016/j.msea.2018.08.072.
[19] M.M. Kirka, D.A. Greeley, C. Hawkins, R.R. Dehoff, Effect of anisotropy and texture on the low cycle fatigue behavior of Inconel 718 processed via electron beam melting, Int. J. Fatigue 105 (2017) 235–243, https://doi.org/10.1016/j.ijfatigue.2017.08.021.
[20] S. Griffiths, H.G. Tabasi, A.D. Luca, J. Pado, S.S. Joglekar, J. Jhabvala, R.E. Loge, C. Leinenbach, Influence of Hf on the heat treatment response of additively manufactured Ni-base superalloy CM247LC, Mater. Charact. 171 (2021) 110815, https://doi.org/10.1016/j.matchar.2020.110815.
[21] S. Griffiths, H.G. Tabasi, T. Ivas, X. Maeder, A.D. Luca, K. Zweiacker, R. Wróbel, J. Jhabvala, R.E. Logé, C. Leinenbach, Combining alloy and process modification for micro-crack mitigation in an additively manufactured Ni-base superalloy, Addit. Manuf. 36 (2020) 101443, https://doi.org/10.1016/j.addma.2020.101443.
[22] J.F.S. Markanday, K.A. Christofidou, J.R. Miller, E.R. Livera, N.G. Jones, E. J. Pickering, W. Li, Y. Pardhi, C.N. Jones, H.J. Stone, The microstructural evolution of CM247LC manufactured through laser powder bed fusion, Metall. Mater. Trans. A 54A (2023) 1758–1775, https://doi.org/10.1007/s11661-022-06939-0.
[23] J.H. Boswell, D. Clark, W. Li, M.M. Attallah, Cracking during thermal post-processing of laser powder bed fabricated CM247LC Ni-superalloy, Mater. Des. 174 (2019) 107793, https://doi.org/10.1016/j.matdes.2019.107793.
[24] V. Kalyanasundaram, A.D. Luca, R. Wróbel, J. Tang, S.R. Holdsworth, C. Leinenbach, E. Hosseini, Tensile and creep-rupture response of additively manufactured nickel-based superalloy CM247LC, Addit. Manuf. Lett. 5 (2023) 100119, https://doi.org/10.1016/j.addlet.2022.100119.
[25] X. Wang, L.N. Carter, B. Pang, M.M. Attallah, M.H. Loretto, Microstructure and yield strength of SLM-fabricated CM247LC Ni-Superalloy, Acta Mater. 128 (2017) 87–95, https://doi.org/10.1016/j.actamat.2017.02.007.
[26] S.E. Atabay, O.S. Mata, J.A.M. Lerma, R. Gauvin, M. Brochu, Microstructure and mechanical properties of rene 41 alloy manufactured by laser powder bed fusion, Mater. Sci. Eng. A 773 (2020) 138849, https://doi.org/10.1016/j.msea.2019.138849.
[27] S.E. Atabay, O.S. Mata, J.A.M. Lerma, M. Brochu, Effect of heat treatment on the microstructure and elevated temperature tensile properties of Rene 41 alloy produced by laser powder bed fusion, J. Alloy. Compd. 858 (2021) 157645, https://doi.org/10.1016/j.jallcom.2020.157645.
[28] K.A. Unocic, M.M. Kirka, E. Cakmak, D. Greeley, A.O. Okello, S. Dryepondt, Evaluation of additive electron beam melting of haynes 282 alloy, Mater. Sci. Eng. A 772 (2020) 138607, https://doi.org/10.1016/j.msea.2019.138607.
[29] S. Singh, J. Andersson, K. Kadoi, Microstructure gradient formation in electron-beam melting powder-bed fusion of a gamma-prime Ni-based superalloy, Mater. Charact. 205 (2023) 113370, https://doi.org/10.1016/j.matchar.2023.113370.
[30] A. Jedynak, A. Sviridov, M. Bambacha, D. Beckers, G. Graf, On the potential of using selective laser melting for the fast development of forging alloys at the example of Waspaloy, Procedia Manuf. 47 (2020) 1149–1153, https://doi.org/10.1016/j.promfg.2020.04.138.
[31] M. Sazerat, A.N. Ali, A. Cervellon, I.L. Galilea, G. Burlot, S. Gillet, D. Eyidi, A. Joulain, P. Villechaise, S. Weber, R. Fortunier, J. Cormier, High temperature microstructure stability of Waspaloy produced by wire arc additive manufacturing, J. Alloy. Compd. 966 (2023) 171626, https://doi.org/10.1016/j.jallcom.2023.171626.
[32] AMS5704L: Nickel Alloy, Corrosion and Heat Resistant, Forgings 57Ni - 19.5Cr - 13.5Co - 4.6Mo - 3.0Ti - 1.4Al - 0.05Zr - 0.006B consumable electrode or vacuum induction melted 1825 to 1900 °F (996 to 1038 °C) solution, stabilization, and precipitation heat treated, SAE International (2020).
[33] Y. Gui, K. Aoyagi, H. Bian, A. Chiba, Detection, classification and prediction of internal defects from surface morphology data of metal parts fabricated by powder bed fusion type additive manufacturing using an electron beam, Addit. Manuf. 54 (2022) 102736, https://doi.org/10.1016/j.addma.2022.102736.
[34] A. Townsend, L. Pagani, P.J. Scott, L. Blunt, Introduction of a surface characterization parameter Sdr prime for analysis of re-entrant features, J. Nondestruct. Eval. 38 (2019) 1–10, https://doi.org/10.1007/s10921-019-0573-x.
[35] L. Pagani, A. Townsend, W. Zeng, S. Lou, L. Blunt, X.Q. Jiang, P.J. Scott, Towards a new definition of areal surface texture parameters on freeform surface: re-entrant features and functional parameters, J. Int. Meas. Confed. 141 (2019) 442–459, https://doi.org/10.1016/j.measurement.2019.04.027.
[36] S.P. Murugan, C. Trainel, A. Oudriss, G. Hachet, F. Danoix, G. Odemer, B. Malard, F. Godet, C. Blanc, X. Feaugas, Some advances on precipitation hardening in Waspaloy: critical review on the contribution of shear, Orowan and coherency mechanisms, Mater. Charact. 216 (2024) 114301, https://doi.org/10.1016/j.matchar.2024.114301.